

ARTICLE OPEN



Cu(In,Ga)Se₂ based ultrathin solar cells the pathway from lab rigid to large scale flexible technology

T. S. Lopes^{1,2,3,4}, J. P. Teixeira¹, M. A. Curado^{1,5}, B. R. Ferreira¹, A. J. N. Oliveira^{1,6,7}, J. M. V. Cunha^{1,6,7}, M. Monteiro¹, A. Violas^{1,6,7}, J. R. S. Barbosa¹, P. C. Sousa¹, I. Čaha¹, J. Borme¹, K. Oliveira¹, J. Ring⁸, W. C. Chen⁹, Y. Zhou⁸, K. Takei¹⁰, E. Niemi¹⁰, F. L. Deepak¹, M. Edoff⁹, G. Brammertz^{2,3,4}, P. A. Fernandes^{1,7,11}, B. Vermang^{2,3,4} and P. M. P. Salomé^{1,6}

The incorporation of interface passivation structures in ultrathin Cu(In,Ga)Se₂ based solar cells is shown. The fabrication used an industry scalable lithography technique—nanoimprint lithography (NIL)—for a 15 × 15 cm² dielectric layer patterning. Devices with a NIL nanopatterned dielectric layer are benchmarked against electron-beam lithography (EBL) patterning, using rigid substrates. The NIL patterned device shows similar performance to the EBL patterned device. The impact of the lithographic processes in the rigid solar cells' performance were evaluated via X-ray Photoelectron Spectroscopy and through a Solar Cell Capacitance Simulator. The device on stainless-steel showed a slightly lower performance than the rigid approach, due to additional challenges of processing steel substrates, even though scanning transmission electron microscopy did not show clear evidence of impurity diffusion. Notwithstanding, time-resolved photoluminescence results strongly suggested elemental diffusion from the flexible substrate. Nevertheless, bending tests on the stainless-steel device demonstrated the mechanical stability of the CIGS-based device.

npj Flexible Electronics (2023)7:4; <https://doi.org/10.1038/s41528-023-00237-4>

INTRODUCTION

Silicon (Si) wafer-based technology dominates the photovoltaic (PV) market share (≈92%), while Cu(In,Ga)Se₂ (CIGS) has only a minor part, with 2%¹. Despite its low market share, CIGS PV shows lower manufacturing costs and material consumption over Si wafer technology, having the potential to be the cornerstone for building-integrated PV (BIPV), due to its applicability for light-weight and flexible applications^{2,3}.

Conventionally, CIGS solar cells are developed using soda-lime glass (SLG) as a substrate. However, SLG is a concern for scalability due to high fabrication costs during module assembly and it also increases the module weight³. Thus, efforts have been made to develop high-efficiency CIGS solar cells with different substrates, such as flexible substrates, that can replace the SLG, mitigating the final device's cost, weight and rigidity. However, the replacement of SLG is complex due to the panoply of requirements that the substrate must meet due to the CIGS composition and growth conditions: similar thermal expansion coefficient with CIGS, thermal stability at high temperatures (>400 °C), chemical inertness with CIGS elements, among others^{4,5}. The prime candidates for flexible substrates are metals and polymers. Metals show high thermal stability but require an additional layer to block elemental diffusion. In contrast, for polymers, only polyimides can withstand temperatures >400 °C, but the thermal expansion coefficient is not compatible with the CIGS one⁵. With these several requirements, breakthroughs in the CIGS technology are usually accomplished with an SLG substrate. Despite the challenges of replacing SLG, the performance of CIGS solar cells performances with flexible substrates are not far from those achieved by SLG ones, as CIGS solar cells on flexible substrates

show an efficiency value of 22.2%⁶, with SLG reaching 23.35%⁷. Furthermore, decreasing the absorber thickness to the ultrathin range (<900 nm) is required to increase fabrication throughput and decrease fabrication costs by reducing the usage of critical raw materials⁸. However, by thinning the absorber, recombination losses at the rear interface became a major loss mechanism. One strategy to tackle those losses is to passivate the rear interface by depositing a dielectric layer between the absorber and the rear electrode^{9–14}. These passivation layers need to be patterned to establish electrical contact. The ideal contact dimensions need to be optimised, considering their geometry and spacing. Nonetheless, a high coverage area by the dielectric is preferred for an efficient passivation^{15,16}. Electron-beam lithography (EBL) and optical lithography have successfully pattern dielectric layers in ultrathin CIGS solar cells^{12,13,15,17}. While optical lithography offers high throughput, its drawback is its low resolution. Although EBL can pattern with high resolution, it suffers from high cost and low direct-write speed, hindering its scalability in the CIGS industry. To leverage the ultrathin CIGS technology, a patterning technique with low cost, high throughput, and high resolution is required. One potential candidate that matches such requirements is nanoimprint lithography (NIL). NIL acts as a parallel patterning method in which a surface pattern, a stamp, is replicated into a material-coated substrate by mechanical contact and 3D material displacement¹⁸. A significant amount of research has been done to explore the NIL capabilities and meet the industry demands since its suggestion by Stephen Y. Chou et al.¹⁹. As a result, NIL is already used in several technologies and industries, such as organic light emission displays, memories, biomedical devices,

¹INL—International Iberian Nanotechnology Laboratory, Avenida Mestre José Veiga, 4715-330 Braga, Portugal. ²Hasselt University, imo-imomec, Martelarenlaan 42, 3500 Hasselt, Belgium. ³Imec, imo-imomec, Thor Park 8320, 3600 Genk, Belgium. ⁴EnergyVille, imo-imec, ThorPark 8320, 3600 Genk, Belgium. ⁵FisUC, Department of Physics, University of Coimbra, P-3004-516 Coimbra, Portugal. ⁶Departamento de Física, Universidade de Aveiro, Campus Universitário de Santiago, 3810-193 Aveiro, Portugal. ⁷i3N, Universidade de Aveiro, Campus Universitário de Santiago, 3810-193 Aveiro, Portugal. ⁸Obducat AB, Medicon Village, 223 63 Lund, Sweden. ⁹Ångström Laboratory, Department of Engineering Sciences, Uppsala University, 751 21 Uppsala, Sweden. ¹⁰Midsummer AB, Elektronikhöjden 6, SE-17543 Järfälla, Sweden. ¹¹CIETI, Departamento de Física, Instituto Superior de Engenharia do Porto, Instituto Politécnico do Porto, 4200-072 Porto, Portugal. ✉email: tomas.lopes@inl.int; jennifer.teixeira@inl.int

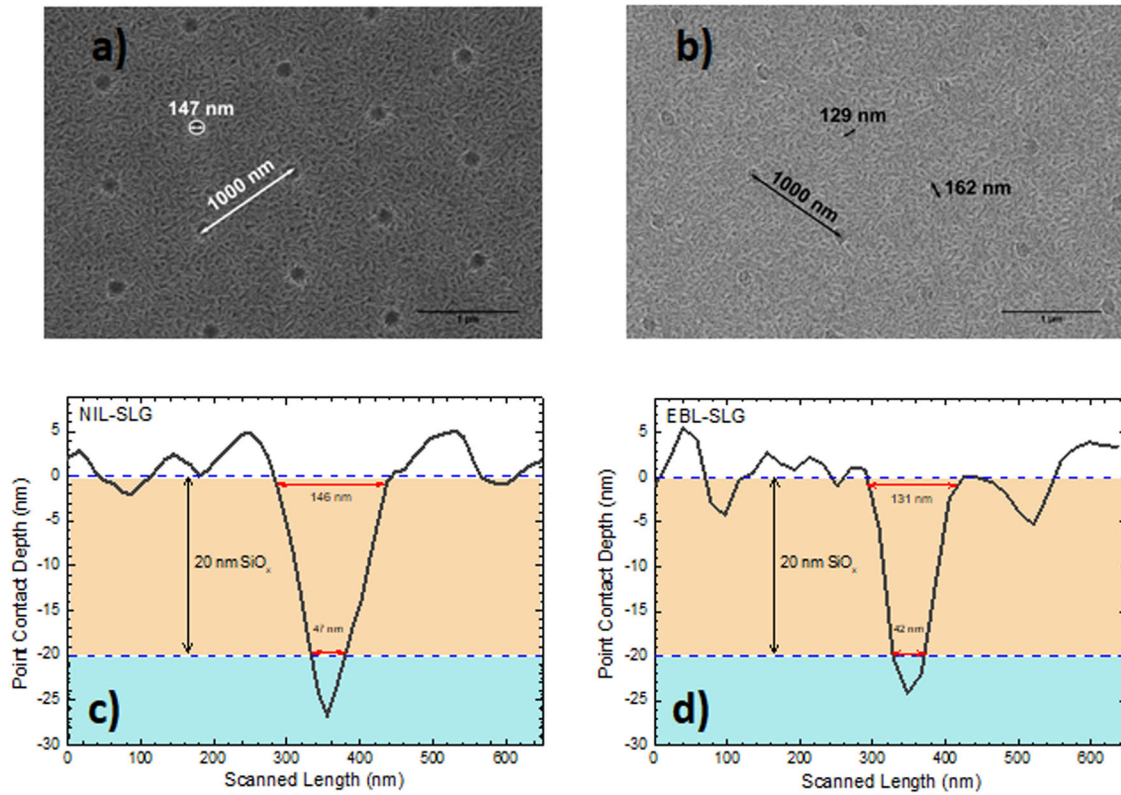


Fig. 1 Rigid substrates morphological characterization after the lithographic process. Top-view SEM images of: (a) NIL-SLG and (b) EBL-SLG substrates. The SEM images were taken with a Horizon field width (HFW) of $5\ \mu\text{m}$ and an acceleration voltage of 5 kV. AFM cross-section profiles of a representative point contact of: (c) NIL-SLG and (d) EBL-SLG substrates obtained with a scan rate of 0.5 Hz. We note that the AFM obtained distance for both substrates is within average values for the SEM measurements.

microelectronics, among others^{20–27}. However, NIL is still to be established in the (ultra)thin film solar cell’s technology.

In order to meet the need for on-site renewable energy, lightweight CIGS based solar cells in flexible substrates are explored in this study with rear passivation by NIL. We studied rigid devices ($5 \times 5\ \text{cm}^2$) with a SiO_x passivation layer patterned by NIL and benchmarked them with devices patterned by EBL. After that, the scalability capabilities of NIL are demonstrated through the patterning of a $15 \times 15\ \text{cm}^2$ semi-squared flexible stainless-steel substrate. Silver (Ag) was incorporated into the CIGS layer (ACIGS), as adding Ag improves crystallinity of thin CIGS devices and allows for low deposition temperatures, matching the requirements of the flexible substrate^{28–30}. The flexible device shows a slightly lower performance than the rigid ones. A set of advanced characterisation techniques was used to understand all the devices, their performance, and to design an experiment to obtain flexible solar cells with a comparable performance to their rigid counterparts. The solar cells’ performance shows the potential for industry scalability for flexible and lightweight ultrathin CIGS based devices, and NIL is a suitable candidate to follow this upscale.

RESULTS AND DISCUSSION

Patterned substrates characterisation

Top view SEM images and cross-section AFM profiles were taken from the NIL-SLG and EBL-SLG substrates to determine the dimensions and profiles of the point contacts. Figure 1a, b show top view SEM images of the NIL-SLG and EBL-SLG substrates, respectively. The average and standard deviation diameter value of 40 point contacts, per substrate, obtained through the SEM top view image analysis is $142 \pm 9\ \text{nm}$ for NIL-SLG and $129 \pm 6\ \text{nm}$

for EBL-SLG. The larger diameter for NIL-SLG likely arises from the O_2 etch process to remove the residual layer, which may enlarge the point contact dimension, due to its isotropic component. On the other hand, EBL-SLG substrate presents point contacts in an elliptical shape caused by astigmatism of the EBL system¹⁷. AFM cross-section profiles of a representative point contact for NIL-SLG and EBL-SLG are shown in Fig. 1c, d, respectively, with the 20 nm SiO_x layer defined between the dashed lines. The AFM cross-section profiles show a complete etch of the SiO_x layer for both substrates and even a minor etch of the Mo layer, ensuring the quasi-ohmic contact between the ACIGS and the Mo layer³¹. From the AFM cross-section profile, the point contact diameter average and standard deviation value for NIL-SLG is $47 \pm 20\ \text{nm}$ and $42 \pm 16\ \text{nm}$ for EBL-SLG. We should note that the difference between the diameter values obtained through top-view SEM images and the AFM profile comes from the etching steps that narrow the point contact into a “V” shape, as the SEM values comes from the top of the contact and the AFM ones are related with the effective interface diameter with the Mo. Nonetheless, the point contacts show similar dimensions for both lithography processes, which is desired since we aimed to have similar architectures, including equivalent over-etching results to minimise the morphological difference between substrates.

The 200 nm Si point contact stamp SEM top view images shown in Fig. 2, were taken during the NIL fabrication to evaluate the process uniformity: (i) the nanoimprinting process—Fig. 2a, b; (ii) the residual layer removal—Fig. 2c and; (iii) the resist removal—Fig. 2d. Figure 2a, b. were taken at opposite edges of the wafer, with a distance of 40 mm, to access the demoulding quality. An imperfect demoulding process leads to elongation in a particular direction³². Figure 2a, b show

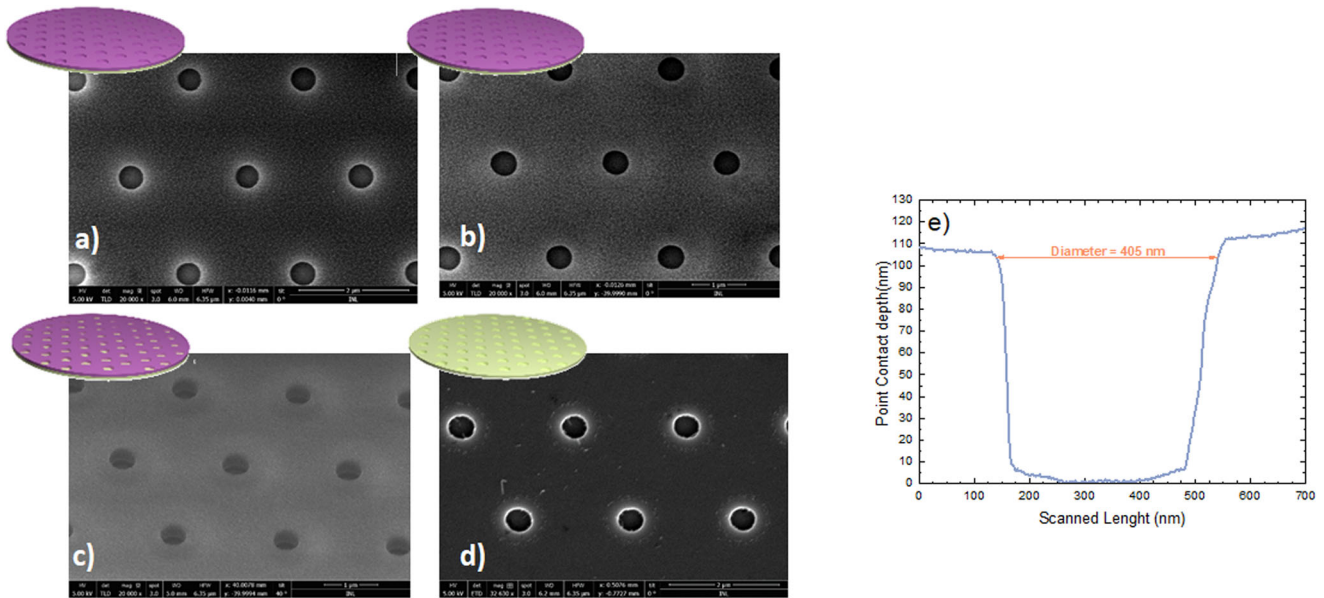


Fig. 2 Characterization of the NIL process on the 200 mm point contact stamp. Top view SEM images of the 200 mm point contact stamp (a) and (b) after the NIL process, (c) after the Si etching, and (d) After the resist removal and wafer cleaning. e AFM cross-section profile of one point contact of the Si stamp.

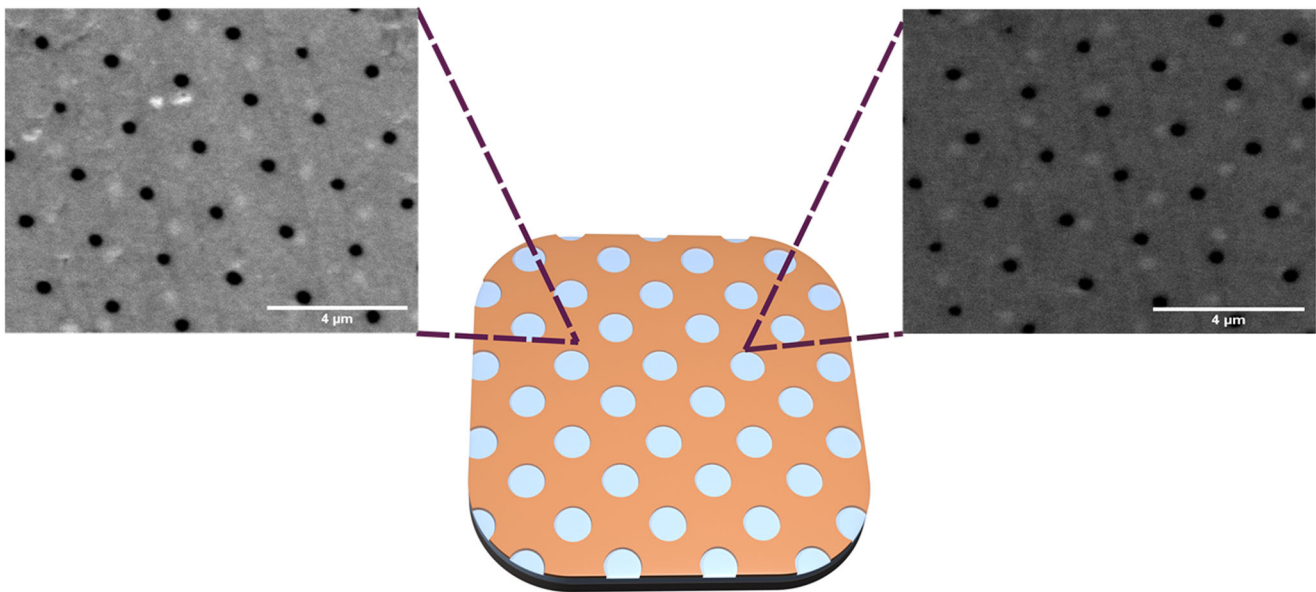


Fig. 3 Flexible substrates characterization after NIL process. Top view SEM images after the resist removal, at opposite sides of flexible substrate, with the identification on the location of the SEM images. The point contact shape and dimension are retained regardless of the distance between the measurement, which indicates high quality for the demoulding step.

clearly defined circular point contacts, with no deformation, and an average dimension of 420 ± 12 nm. From the point contact presented in Fig. 2e, the point contact seems to have well defined vertical sidewalls with a depth of 110 nm and a diameter of 405 nm, compatible with the SEM top view dimension. These results support the uniformity of employing NIL to perform a double polarity inversion in the 200 mm fabricated stamp, and the high quality of the produced stamp to pattern the large scale solar cell.

The patterning process of the Flexible highlights the industrialisation aspect of NIL, as the imprinting step took only 7 min. However, exposing the same pattern with EBL would take up to 8000 min of non-interrupted machine runtime. NIL on non-flat surface substrates, such as steel, commonly employs high pressure

to overcome the surface roughness¹⁸, hence SEM top-view images are mandatory to check the uniformity of the process¹⁸. Figure 3 shows the top-view SEM images of Flexible at opposite sites on the substrate after the resist removal process. From the top view SEM images, the point contacts show well-defined and circular dimensions, indicating a successful demoulding. An uniformity in shape geometry in the whole sample is important as demoulding can lead to artefacts in the shape of the features, as that is not the case here, we can conclude that the demoulding has no issues. The average diameter for the point contacts obtained by SEM images is 391 ± 39 nm. The uniformity of the point contacts shape indicates that our STU-NIL process and the use of a flexible IPS® can overcome the surface roughness of the steel wafer, leading to uniform features.

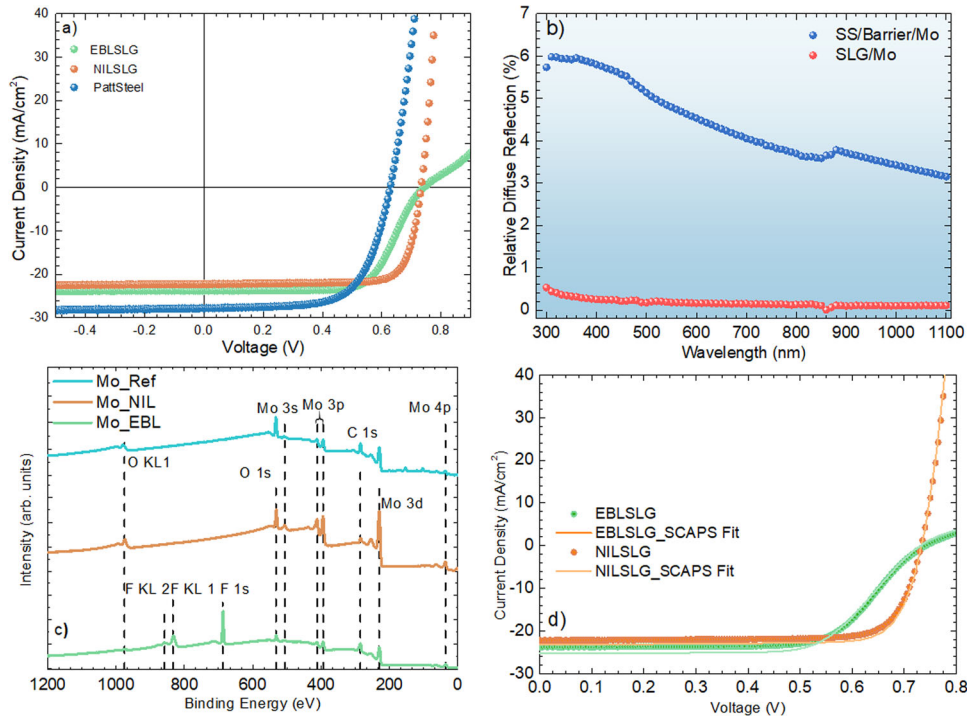


Fig. 4 Solar cell results of the fabricated devices. **a** Representative illuminated J - V curves; **b** Relative total diffuse reflection of Mo into a SLG and Stainless-steel substrate; **c** XPS survey spectra of Mo based substrates without etch process, Mo_Ref, and with a BCl_3 and C_4F_8 based etch process for substrate Mo_NIL and Mo_EBL, respectively are shown; **d** SCAPS fit to the EBL-SLG and NIL-SLG illuminated J - V curves presented in **a**.

Table 1. The figures of merit average and standard deviation values for the fabricated devices and in dark blue the one obtained via SCAPS fit for EBL-SLG and NIL-SLG, additionally the rear barrier for holes, and the SRV for electron and hole are also presented.

Devices	V_{OC} (mv)	J_{SC} (mA/cm^2)	FF (%)	Efficiency(%)	Barrier (eV)	e-SRV ($\text{cm}\cdot\text{s}^{-1}$)	h-SRV ($\text{cm}\cdot\text{s}^{-1}$)	R_s ($\text{ohm}\cdot\text{cm}^2$)
EBL-SLG	744 ± 3	24.0 ± 0.3	68.6 ± 2.7	12.3 ± 0.5				
NIL-SLG	730 ± 2	21.7 ± 0.5	79.2 ± 0.6	12.6 ± 0.4				
Flexible	628 ± 3	27.9 ± 0.5	66.8 ± 0.3	11.7 ± 0.3				
EBL-SLG	730	25.3	66.3	12.3	0.140	$1.07\text{E} + 02$	$1.60\text{E} + 02$	2.88
NIL-SLG	734	23.3	80.2	13.7	0.160	$1.00\text{E} + 04$	$1.00\text{E} + 04$	0.085

Solar cells results

The three studied devices' representative illuminated J - V curves and figures of merit average values are presented in Fig. 4a and in Table 1, respectively. The average power conversion efficiency values obtained for SLG substrates are very close, 12.6 and 12.3% for NIL-SLG and EBL-SLG devices, respectively. Nevertheless, a slight decreased value is obtained when moving to the large area flexible stainless-steel based device, 11.7%, even though it is a <1% conversion efficiency decrease. Such results highlight the potential of the developed process to include large flexible substrates in the CIGS based ultrathin solar cells portfolio^{13,33–35}. The EBL-SLG device shows a roll-over behaviour, responsible for its FF value lower than NIL-SLG. This roll-over anomaly likely indicates a presence of an electronic barrier^{36,37}, which might be related with Na distribution problems^{36,38}. Nonetheless, in the NIL-SLG device—which has the same pattern and received the same amount of NaF precursor—the said rollover is absent. Remarkably, the NIL-SLG device achieved a FF value of 79.2%, which is higher than the FF values obtained in high efficiency sub-micrometre CIGS-based solar cell devices^{39,40}, albeit 1.2% lower than the one achieved in the current world record CIGS based thin film solar cell⁷. Nonetheless, an absolute decrease of 12.4% in the FF value is

Table 2. Description of the samples' nomenclature, the thickness of the passivation layer, lithography used and the rear stack.

Substrate/ Device name	Lithography technique	Dielectric layer thickness (nm)	Rear stack
EBL-SLG	EBL	8	SLG/Mo/ SiO_x
NIL-SLG	NIL	20	SLG/Mo/ SiO_x
Flexible	NIL	20	Steel/Mo/ SiO_x

observed for the Flexible device when compared to the NIL-SLG. This loss might be explained by the high roughness present in the steel substrate and by the difficulty in cell definition. AFM measurements show a root mean square surface roughness of 18.6 nm for the stack Steel/Mo, ~300% higher than the one obtained for the SLG/Mo which is 4.9 nm. Notwithstanding, we highlight the low standard deviation values (Table 2) for the Flexible devices, indicating the high uniformity of the individual solar cells. The Flexible devices show the highest J_{SC} values amongst the fabricated solar cells, which may come from light trapping effects due to the steel surface roughness, which will

increase the optical path length inside the device, thus increasing the J_{SC} value³³. Relative diffuse reflectance measurements of Steel/Mo and SLG/Mo substrates are presented in Fig. 4b. A broadband increase is observed for the stainless-steel substrate. However, the light trapping effect evaluated through the inclusion of the obtained surface roughness in the solar cells architecture via 3D finite-difference time-domain optical simulations⁴¹, shows a lower J_{SC} enhancement than the one measured. Thus, optical phenomena are insufficient to solely explain the difference between the J_{SC} of the Flexible and the SLG based devices⁴². Considering the SLG devices, a difference on the J_{SC} value of 2.3 mA cm^{-2} was obtained, while keeping 98% of the EBL-SLG V_{OC} value, the NIL-SLG device presents an unexpected decrease in the J_{SC} . So far, the obtained results show two main differences between the SLG solar cells; a 2.3 mA cm^{-2} J_{SC} difference between them, and a roll-over anomaly in the EBL-SLG suggesting charge extraction problems. These differences are unexpected as the substrate architecture is nominally the same, as well as the upcoming layers and its processing, including the absorber. We relate this difference to two major points: a non-uniform distribution of the Na doping, although both samples have the same NaF thickness, and/or the effectiveness of the passivation layer (chemical and field-effect passivation effects). Both these points should have somehow a connection to the lithographic process and its operational conditions—exposure, resists, and more importantly the chemical nature of the etch process, which was different for the two SLG based substrates. As the two SLG lithographic procedures required different etch processes, which inevitably led to different by-products, XPS surveys were performed on three Mo based samples that mimic the etch by-products. Thus, SLG sputtered 350 nm Mo substrates were submitted to equal etching conditions together with the same cleaning steps for the correspondent devices. Hence, Mo_EBL was etched in a C_4F_8 based chemistry for 45 s in an APS system at a pressure of 2.6×10^{-6} bar with a flow of 50 sccm at 13.56 MHz, and Mo_NIL with a BCl_3 based chemistry for 50 s at a pressure of 2.6×10^{-6} bar with a flow of 15 sccm at 13.35 MHz, with Mo_Ref being submitted to only cleaning steps. We note that the survey was conducted on a bare Mo substrate, without dielectric and nanopatterning. However, the identification of elements in the Mo substrate should follow the detention of elements on a Mo surface in a patterned device, despite a possible overestimation by XPS in non-patterned substrates. All the XPS surveys spectra are presented in Fig. 4c. A major difference stands out: the Mo_EBL spectrum shows a fluor (F) contribution. None of the other samples show the presence of F. The F appears as by-product of the C_4F_8 based etch used in the EBL sample. Despite the existence of F on the Mo_EBL surface, we note the presence of Carbon (C) and Oxygen (O) peaks with varied intensity between the samples. Such peaks may appear due to sample handling and exposure to air. No detrimental impact is expected by the presence of F in the EBL-SLG sample, as every studied sample had a NaF treatment, and this element is commonly used both in alkali-precursors in post-deposition treatments³⁶. Moreover, it is not expected that F had an impact in the observed barrier in the EBL-SLG device, since the roll-over behaviour was also previously observed in devices with substrates architectures obtained through BCl_3 etch¹⁵. Furthermore, a closer inspection to the F 1s spectra, not shown, has the presence of two peaks: one at 688.2 eV, and a small shoulder with a peak 684.6 eV. The former indicating the presence of an organic compound⁴³ with the latter being an inorganic⁴⁴. The organic compound may have formed due to a reaction of the etching gases during the process, with the inorganic compound being formed with a reaction of F to the Mo layer. Such compounds may react and potentially affect the NaF dissociation and chemistry during the CIGS growth and the relation between Na, O, F and Se and Na diffusion is quite complex^{45,46}. Hence, an in depth study of how these compounds may affect Na distribution

and even the NaF dissociation should be conducted. Moreover, SCAPS software was used to further discuss the SLG-based devices. The implementation of an 1D Poisson solver along with complex architectures that may not be totally described by the one-diode model, bring an additional complexity in the deconvolution and discussion of the electrical parameters. In order to better describe the developed architectures, the SCAPS model was fitted to the EBL-SLG and NIL-SLG measured $J-V$ curves, as shown in Fig. 4d, by varying the rear contact barrier (i.e. contact work function) and the surface recombination velocity (SRV) for electrons and holes, in order to achieve the lowest Chi-square sum value. The fitted figures of merit are presented in Fig. 6b. This model was implemented for five scenarios of compensation varied from 17 to 67% in the bulk region, where (1) the rear contact transport barrier height was varied from 0 to 0.3 eV since a roll-over effect was observed in the EBL $J-V$ curve, and (2) the SRV for electrons and holes were varied from 10^4 to 10^2 cm/s, as the rear passivation effect on SRV observed experimentally typically varies within such range values^{47,48}. An important result comes from the compensation level that better describes the $J-V$ curves, which is 11% (abs.) higher for the EBL-SLG comparing to the NIL-SLG. This result is compatible with a more efficient integration of Na in the NIL-SLG device, raising the point that having additional F in the substrate may difficult the NaF dissociation and consequently the incorporation of Na on the ACIGS. Additionally, it is known that the Na presence is a prerequisite as a catalyst to the $MoSe_2$ formation providing a quasi-ohmic contact⁴⁹, which might explain the higher simulated series resistance (R_s) value for the EBL-SLG device. No significant rear barrier height was obtained for both devices. Therefore, the charge accumulation responsible for the roll-over effect might be related to other phenomena. Note that, the AFM measurements revealed that in the EBL-SLG solar cell the average individual contact area is 20% lower than the NIL-SLG one, in addition the hole (h)-SRV obtained value for this device suggests a higher hole density available to be extracted, which may lead to charge accumulation at the rear contact in the EBL-SLG solar cell. The accumulation of both effects leads to a series resistance increase revealed by a roll-over effect. The fitted figures of merit show lower SRV values for the EBL-SLG in comparison to the one obtained for the NIL-SLG. The presence of F in the Mo layer may create an additional field effect, allowing for an improvement in the J_{SC} value. Notwithstanding, the SRV values must also reflect the slight differences in the passivation architecture dimensions. Although, an improved rear interface passivation effect might be obtained by the presence of F, it also affects the NaF dissociation and the compensation values, and therefore the optoelectronic properties of the ACIGS, leading to similar V_{OC} values between both devices. Furthermore, given that the Flexible device also went through an etching process based on C_4F_8 and given its high J_{SC} values, it is possible that for this sample the presence of F in the Mo surface together with the higher diffuse reflectance may be responsible for its high J_{SC} . However, a detrimental impact in the optoelectronic properties of the ACIGS is expected, which will affect the V_{OC} value. Nonetheless, the large V_{OC} drop observed in the stainless-steel device might not be fully explained by this effect, as it was seen that in the SLG-based devices the V_{OC} values are similar.

It should be noted that the SLG based CIGS solar cells commonly show higher V_{OC} values than those achieved by stainless-steel substrates^{50,51}, thus, the lower V_{OC} value for Flexible solar cells is an expected but unwanted result. Common causes for such difference may come from diffusion of elements present in the steel substrate, such as iron (Fe), towards the CIGS^{51,52}, which might have occurred due to the used CIGS growth temperature⁵⁰. The small drop in the overall Flexible performance is mostly due to the significant decrease in the V_{OC} values. Thus, despite of the diffusion barrier and the SiO_x passivation layer, some impurities may still diffuse towards the absorber. Thus, cross-section STEM

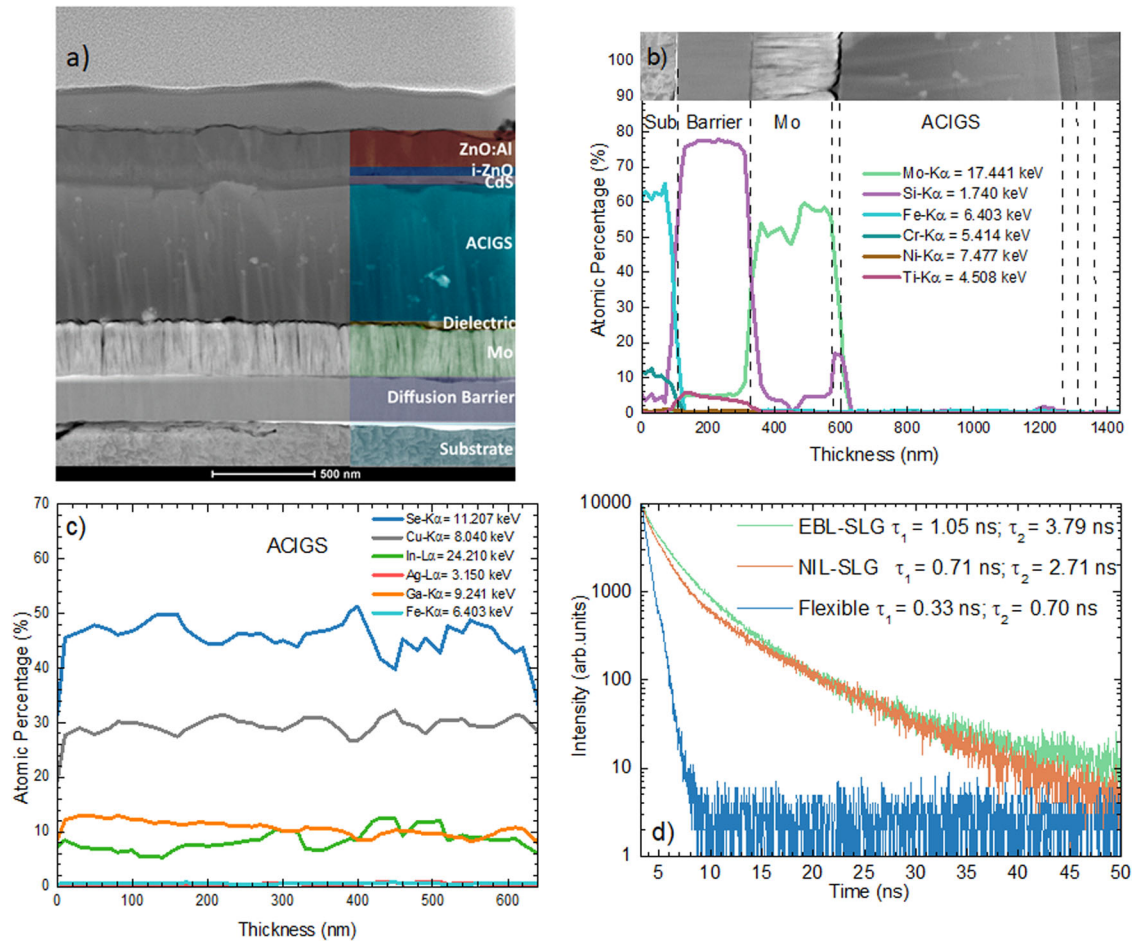


Fig. 5 Flexible device characterization by STEM and TRPL. STEM and EDS graph for the flexible device **a** cross section STEM image for Flexible device with the corresponding layers of the device identified; **b** EDS line scan for the complete device. For clarity, only the elements present in the substrate, diffusion barrier and Mo contact are shown. The EDS line scan region is shown in the image; **c** EDS line scan in the ACIGS layer, where the corresponding elements together with Fe are shown; **d** room temperature TRPL decay for EBL-SLG, NIL-SLG and Flexible. A double exponential decays is observed for all substrates.

images and EDS line scans were taken for the Flexible device to study the elemental distribution in the ACIGS layer. Figure 5a shows a cross section STEM image for Flexible device, with Fig. 5b, c showing the EDS line scan profile for the substrate's elements throughout the complete device and the ACIGS elements plus Fe in the absorber layer, respectively. The STEM image shows a conformal layer growth of the solar cell stack layers. The complete device's line scan in Fig. 5b initially shows a high signal from elements present in the steel substrate, such as Fe and chromium (Cr), with Fe having the highest atomic percentage. A residual percentage of titanium (Ti) and nickel (Ni) was also detected into the stainless-steel substrate, while an increase in the atomic percentage of Ti was observed in the barrier region. The Si signal detected supports the SiO_x based nature of that barrier. Moreover, once we reach the diffusion barrier, we observe a decrease of Fe and Cr elements, as Ni, Ti, and Cr reach a near zero atomic percentage at the Mo layer. Such a drop in atomic percentage indicates that the diffusion barrier together with Mo significantly prevented further diffusion of these elements onto the CIGS. Note that, at the Mo/ACIGS interface the Si signal increases. This phenomenon is explained due to the proximity between the Si $K_{\alpha} = 1.740$ keV and the Se $L_{\alpha} = 1.379$ keV, which indeed reflects the common formation of the nanometric MoSe_2 interfacial layer³¹. The elemental distribution in the ACIGS layer (Fig. 5c) follows the trend expected for an inline deposition process. Furthermore, we note that the ACIGS elemental distribution

observed by STEM may show some variations from the one measured by XRF. Such difference results from experimental artefacts, such as Cu grid on the lamella, Ga implantation from the lamella preparation and addition experimental error from the techniques. The Fe element was also scrutinized in this layer. However, only a very residual presence of Fe was detected, which does not allow for a clear conclusion considering its presence in the absorber, since it may be an artefact. In this regard, TRPL measurements were performed in order to evaluate possible differences in the recombination mechanisms between devices. The TRPL decay of the three studied samples is presented in Fig. 5d, being all well described by a biexponential function with two characteristic decay lifetimes^{53–55}: τ_1 is often linked to charge separation and τ_2 to recombination mechanisms. A clear difference in the TRPL decay is observed between the SLG based devices and the stainless-steel one, which presents a faster decay in comparison to its SLG counterparts. Both SLG devices present similar decay curves, with slightly higher τ_1 and τ_2 values for the EBL-SLG in comparison to the NIL-SLG. The trend of the τ_2 values from these two solar cells is well aligned with the one from the V_{OC} values, both parameters showing a small gain for the EBL-SLG. Thus, no significant differences on the optoelectronic properties were found between the two SLG solar cells. Despite the many physical factors that may determine the TRPL decay, the significant change observed in the Flexible decay, strongly indicates additional non-radiative recombination mechanisms

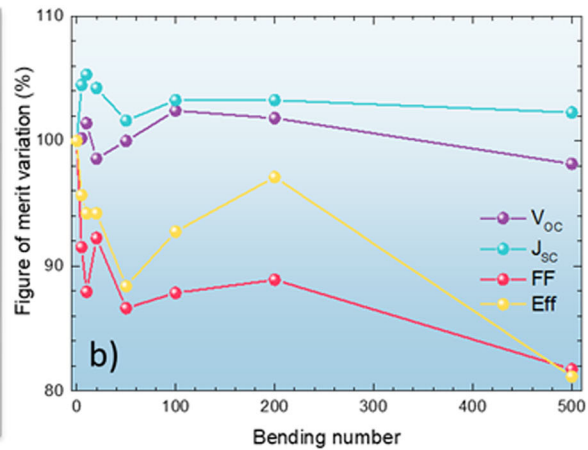
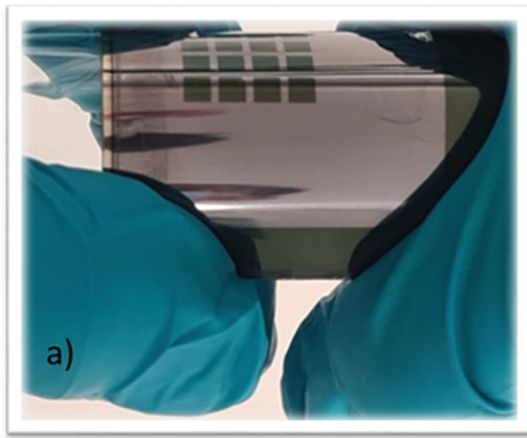


Fig. 6 Mechanical bending of the flexible device. **a** Photography of the bent Flexible device; **b** Flexible figures of merit variation as a function of the bending cycles.

that are not present in the rigid devices, which is compatible with the low V_{OC} value obtained for the Flexible solar cell. Therefore, elemental diffusion from the stainless-steel substrate at doping levels which are not detected by EDS might have diffused towards the ACIGS leading to additional non-radiative recombination channels, which might explain the much faster TRPL decay in the Flexible device in comparison to the rigid solar cells. Moving forward, the development of either new diffusion barriers and/or using a thicker Mo layer⁵¹ should be developed to completely block metal diffusion towards the absorber, as it allows for a smoother transaction between laboratory devices and industry. Moreover, additional growth optimisation of CIGS based layers at low temperatures could also help to mitigate said issue^{30,56}.

In order to study the mechanical stability of Flexible device (Fig. 6a), we calculated the applied strain, ϵ , on the device surface as it allows for the description of the physical device deformation during the bending^{57,58}:

$$\epsilon = \frac{t}{2R} \quad (1)$$

where, t is the total thickness of the device, being $114\ \mu\text{m}$ (substrate included) and R the bending radius, $14.4\ \text{mm}$. Thus, a strain of 0.4% is induced in the devices when bent. Figure 6 shows a small variation in the J_{SC} and V_{OC} value throughout the bending tests, which might be due to an artifact resulting from the $J-V$ setup optimized for flat devices. Still the fact that the parameter did not degrade indicates that: (i) the mechanical strain did not lead to a change in the ACIGS lattice; and (ii) the optical properties were unaffected by mechanical deformation. However, the FF and efficiency values decreased in the first 50 bending cycles, while stabilising for the subsequent bending cycles. Studies show that FF might decrease in solar cells during bending measurements due to a deterioration in the window layer properties^{59–61}. In fact, the ZnO based window layer used in our device is compatible with previously reported poor mechanical stability, since only a few bending cycles are needed to break down the material properties^{62,63}. Hence, the cause for performance loss in our devices could be the degradation of the window layer properties, with the exact cause being the subject of further studies. For flexible applications, where mechanical stability is of utmost importance, a different TCO should be used, such as Ag nanowires together with thin AZO, which demonstrated higher mechanical stability compared to standard TCO layers^{64,65}. Nonetheless, the stable V_{OC} and J_{SC} shows the mechanical robustness of the electrical and optical properties of ultrathin CIGS based layer on stainless-steel substrates. The solar cell results of Flexible and NIL-SLG show that NIL can pattern devices with efficiency values

close to the well-established EBL process. The results of the Flexible device indicate that with the correct patterning technique, together with an optimized growth process, ultrathin flexible devices may reach the performance of rigid substrates.

The pathway for the development of high-performance ultrathin flexible solar cells was established in this work. As ultrathin devices need the incorporation of a patterned passivation layer, we show that NIL processing is fit for both patterning the necessary structure and flexible substrates. Firstly, the NIL process was compared to a well-established lithography approach, EBL, in rigid substrates, followed by the patterning of a large area flexible substrate ($15 \times 15\ \text{cm}^2$). SEM and AFM analyses demonstrated the NIL uniformity on a $200\ \text{mm}$ wafer and over an area of $15 \times 15\ \text{cm}^2$, as well as the reproducibility between lithographic processes. Rigid devices demonstrated similar performances. Despite the similar TRPL decay lifetimes and V_{OC} values, the EBL patterned device showed a higher J_{SC} value, and a roll-over effect leading to a lower FF, compared to the NIL patterned device. XPS survey measurements showed the presence of F in Mo substrates etched by C_4F_8 based chemistry, being this element a by-product of the etch procedure used in the EBL device. The measured $J-V$ curves were fitted with SCAPS, revealing different levels of compensation in the ACIGS layer, and R_s and SRV values. These variations might be explained by the presence of F in the EBL device substrate, highlighting that the etch process of the patterning might be important for device performance. Furthermore, similar rear contact barrier values were obtained for both devices, therefore the roll-over effect was linked to charge accumulation, brought by the lower contacting area and h-SRV value for the EBL device. Nonetheless, the complexity of the simulated architectures along with the 1D nature of the simulation software might not be sufficient to explain the fit parameters through a one-diode model vision and more studies of the rear interface recombination are generally needed. The flexible device had a power conversion efficiency value of 11.7% , slightly lower, albeit not a significant performance decrease, compared to the rigid devices. The flexible stainless-steel performance reflects the high ACIGS growth temperature, which might have promoted the diffusion of detrimental elements towards the absorber, which could also explain the TRPL sharper decay for the flexible device as opposed to the rigid ones. If present, Fe, is at a concentration too low to be clearly identified with STEM-EDS. However, the ACIGS absorber is extremely sensitive to Fe impurities and as such future works should work in understanding if there is really Fe diffusing and in alternative approaches to mitigate said diffusion. The high steel surface roughness values usually leads to lower FF values, in

accordance to what was observed in this work. The flexible device showed excellent mechanical properties as the performance after 500 bending cycles showed only an 18% variation to before bending and this degradation being likely linked to the TCO layer. As such, future studies of flexible substrates should be focused on improving diffusion barriers, processing, lowering roughness and making the TCO layer less prone to mechanical damage. All in all, we showed the successful implementation of rear passivation strategies in a lightweight large area flexible device, which is critical to the development of the CIGS technology in non-traditional PV markets.

METHODS

Three ultrathin CIGS based devices were fabricated: two SLG-based and one with a flexible stainless-steel substrate. For the case of SLG-based substrates, two different patterning techniques were compared: one substrate was patterned by EBL (EBL-SLG) and the other one by NIL (NIL-SLG). Afterwards, a $15 \times 15 \text{ cm}^2$ flexible stainless-steel substrate was patterned using a NIL process (Flexible). Table 2 summarizes the fabricated devices with the description of the fabricated substrates. Given the dimensions of the stainless-steel substrate, a NIL stamp able of patterning such large area was developed. SiO_x passivation layers with 8 and 20 nm were deposited on a Mo contact (350 nm) for the steel and in the SLG based substrates, respectively, through plasma-enhanced chemical vapour deposition (PECVD) in an SPTS MPX CVD system^{31,35,66}. A thinner SiO_x for the Flexible sample was chosen, since a lower thickness is more suitable for flexible applications⁶⁷. The SiO_x layer thickness was estimated by an OPM NanoCalc optical profilometry system.

SLG based substrates lithography

Figure 7 shows a schematic of the lithography process for the SLG-based substrates coated with SiO_x . We used the same pattern architecture for both substrates for comparison purposes: 100 nm point contacts diameter with $1 \mu\text{m}$ pitch in a hexagonal array. The pattern dimensions were chosen to balance a high dielectric coverage area with a low EBL exposure time¹⁵. The EBL procedure started with spin-coating an electron sensitive resist, 430 nm of Polymethyl methacrylate (PMMA) (Fig. 7b), followed by an exposure step (Fig. 7c.2) using an acceleration voltage of 100 kV in a Vistec 5200 system. Then, the pattern was developed for 40 s using a Methyl isobutyl ketone (MIBK) developer diluted in Isopropanol (IPA). Afterwards, the exposed SiO_x layer was opened by Reactive Ion Etching (RIE) (Fig. 7e) in an STPS Advanced Plasma System (APS) at 13.6 MHz in C_4F_8 chemistry with a flow of 50 sccm for 45 s. Finally, the remaining PMMA was removed (Fig. 7f) by immersing the substrate in an ultrasound bath in acetone. For the NIL patterned substrate, the process started by spin-coating a Simultaneous Thermal and UV (STU[®]) resist (TU7-120, Obducat) with a thickness of 150 nm (Fig. 7b). Before the imprint, the hexagonal array contact pattern was transferred from a 100 mm nickel stamp to an Intermediate Polymer Stamp (IPS[®]) by UV-NIL. The use of IPS[®] extends the initial stamp lifetime and enables to work with UV for non-transparent substrates and moderate pressures^{32,68}. A UV-NIL process was conducted to transfer the pattern to the IPS[®], in a NanoImprint Eitre 6 system (Obducat AB). Initially, the pressure was raised to 15 bar for 30 s, followed by UV exposure for 180 s, while maintaining the pressure. Subsequently, the IPS[®] was rolled to the substrate for the imprint. The imprint started with increasing the stage temperature to 65°C with a pressure of 15 bar for 80 s. Then the UV light was turned on for 180 s, while maintaining the temperature and pressure (Fig. 7c.1). A 70 nm residual TU7-120 resist layer was removed by O_2 etch in an STPS Pegasus system for 5 s with an O_2 flow of 115 sccm at 13.56 MHz (Fig. 7d.1). Then, RIE was used to open the point

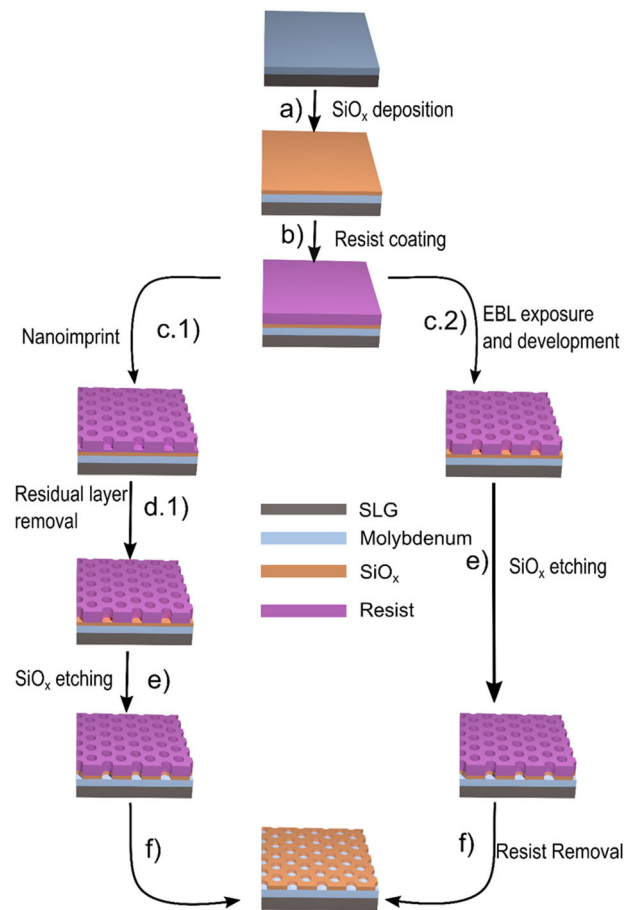


Fig. 7 Rigid substrates lithography process. Schematic representation of the lithography process for patterning SLG-based substrates with NIL (Left) and EBL (Right). The fabrication steps are as follows: (a) SiO_x deposition; (b) Resist coating; (c) Lithography exposure; (d) Residual layer removal; (e) SiO_x etching; and (f) Resist Removal. Schematic, not at scale.

contacts in an STPS Inductively Coupled Plasma Source (ICP) system for 50 s in a BCl_3 chemistry with a flow of 15 sccm at 13.56 MHz (Fig. 7e). The resist layer was stripped by O_2 plasma ashing with an O_2 and Ar flow of 200 sccm and 20 sccm, respectively (Fig. 7f).

Flexible stainless-steel substrate master stamp fabrication and lithography

The fabrication of a 200 mm Si stamp with point contacts was divided into two lithographic processes: (i) EBL, to produce 400 nm wide nano-pillars, with the same EBL procedure as described elsewhere⁶⁹; and (ii) NIL, to invert the stamp polarity from pillars to point contacts. Figure 8 shows a schematic of the workflow for a two-step polarity inversion process to manufacture a 200 mm point contact Si stamp from a Si pillar stamp. This workflow requires two polarity inversion processes, which involves two distinct working stamps, namely an Ormostamp polymer (Micro-Resist Technology GmbH) and an IPS[®], which results in a point contact and a pillar pattern, respectively.

The first polarity inversion was conducted by dispensing an Ormostamp droplet on a Si pillar stamp, placing a glass wafer on top of the Ormostamp and squeezing it for a uniform distribution at 5 bar for 300 s, followed by UV exposure for 35 s, obtaining a point contact structure in this intermediate stamp (Fig. 8a). After the transfer process, 70 nm of an anti-sticking layer was deposited on the Ormostamp surface in an STPS Pegasus system

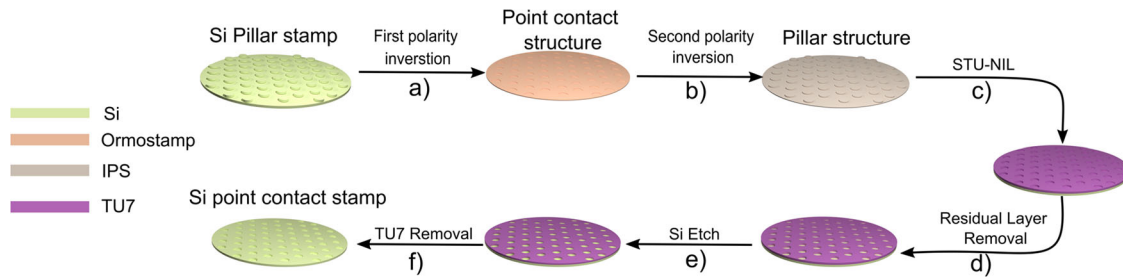


Fig. 8 200 nm point contact stamp replication process. Schematic with the 200 mm point contact Si Stamp fabrication steps. Not at scale.

for 10 s with 13.56 MHz in a C_4F_8 chemistry. For the second polarity inversion an IPS[®] was rolled into the Ormostamp surface, followed by a UV-NIL step. For this process, the pressure was raised to 15 bar for 30 s with no UV, followed by UV exposure for 180 s while maintaining the pressure, obtaining a pillar structure on the IPS[®] (Fig. 8b). The fabrication process of the Si point contact stamp was then performed through a STU-NIL process using the IPS[®] pillar intermediate stamp. For that, the IPS[®] was rolled on a Si wafer coated with 500 nm of TU7—310 Obducat resist. In the STU-NIL step, the temperature and pressure were raised to 65 °C and 15 bar and maintained for 80 s, followed by UV exposure for 180 s, while maintaining the above conditions (Fig. 2c). The resulting residual layer was 100 nm and was removed with an 8 s O_2 etching process in an STPS Pegasus system (Fig. 8d) and followed by an etch of the Si layer by 110 nm in an STPS ICP system (Fig. 8e). At the end of the etching process, the remaining resist was stripped with O_2 plasma ashing (Fig. 8f).

The lithography process for the flexible stainless-steel substrate, with a hexagonal array of 400 nm point contacts with a pitch of 2 μ m follows the NIL procedure shown in Fig. 7. We used the Si stamp described above for the stainless-steel substrate imprinting. For the lithography process, the wafer was coated with 160 nm of TU7-120 resist (Fig. 7b). Before the imprint, the pattern in the Si stamp was transferred to an IPS[®], by UV-NIL for 180 s at 10 bar, the Si stamp was coated with an anti-sticking layer to ease the demoulding in an STPS Pegasus system. After the transfer, an anti-sticking layer was deposited on the IPS[®] surface in an STPS Pegasus system. The imprint conditions were done with the same parameters as the SLG-based substrate (Fig. 7c.1). The resist residual layer was removed with an O_2 etch in an SPTS Pegasus system for 5 s with an O_2 flow of 115 sccm (Fig. 7d.1). Afterwards, RIE was used to open the point contacts in an SPTS APS for 20 s (Fig. 7e). The remaining resist layer was removed through an O_2 plasma ashing (Fig. 7f).

Solar cell integration

After the lithography processes, all the substrates from both sets were integrated into ultrathin ACIGS based solar cells. Before the ACIGS growth, a 15 nm Sodium fluoride (NaF) was evaporated on all substrates. The ACIGS was grown in a one-stage co-evaporation process. Two references samples based on Substrate/Mo/ACIGS were grown in the same deposition run as the fabricated devices (one per run) and were used for elemental distribution using X-Ray Fluorescence (XRF) For the SLG glass substrates, the estimated ACIGS thickness was 720 nm with $[Ag]/([Ag]+[Cu])/([Ga]+[In]) \approx 0.82$, $[Ga]/([Ga]+[In]) \approx 0.40$, and $[Ag]/([Ag]+[Cu]) \approx 0.09$. For the flexible stainless-steel substrate the ACIGS layer had an estimated thickness of 650 nm, with $[Ag]+[Cu]/([Ga]+[In]) \approx 0.88$, $[Ga]/([Ga]+[In]) \approx 0.43$, and $[Ag]/([Ag]+[Cu]) \approx 0.12$, as determined by X-ray fluorescence (XRF) performed in a Panalytical Epsilon 5, with a maximum 5% elemental composition variation⁷⁰. After the growth of the ACIGS layer, the remaining CdS/i-ZnO/ZnO:Al layers were fabricated

following the Ångström baseline standard process⁷⁰. Per device, 12 solar cells with an area of 0.1 cm² were individualised by a lithography process.

Substrates and solar cells characterisation

Scanning Electron Microscopy (SEM) was used for top view images of the substrates with acceleration voltages of 3 kV and 5 kV in a NovaNanoSEM 650 FEI system. Before the ACIGS growth, the substrates' architectures were analysed, by a Bruker Icon Atomic Microscope (AFM) in tapping mode with a scan rate of 0.5 Hz. Completed solar cells were characterised by current-density against voltage (J - V) measurements with an AM1.5G illumination source at 1000 W.m⁻², performed in a home-built system. Bending cycles were conducted manually in a tube with a 14.4 mm radius. In total, 500 bends were performed, and illuminated J - V measurements were conducted before bending and after 1, 5, 10, 20, 50, 100, and 500 bending cycles, after returning the device to a planar state. An ESCALAB[™] 250Xi (Thermo Scientific[™]) XPS system was used for the substrate surface survey measurement, with an X-ray monochromatic source of Al K_{α} (1486.86 eV). The measurements conditions were used with a pass energy of 200 eV and, a dwell time of 300 ms, three repetitions, and a scan region between 0 eV and 1200 eV was carried out. Scanning Transmission Electron Microscopy (STEM) with energy-dispersive X-ray spectroscopy (EDS) was conducted on the Flexible device in a probe-corrected FEI Titan G2 ChemiSTEM equipped with a Super-X EDX System, operating at 200 kV. The device lamella was prepared by focused ion beam (FIB), in a Cu grid, prepared in a FEI Dual-Beam Helios 450 S. For the EDS maps, the following elements and their corresponding characteristic emission spectrum lines were chosen: Fe K_{α} = 6.403 keV, Cr K_{α} = 5.414 keV, Ni K_{α} = 7.477 keV, Ti K_{α} = 4.508 keV, Si K_{α} = 1.740 keV, Mo K_{α} = 17.441 eV, Ag L_{α} = 3.150 keV, Cu K_{α} = 8.040 keV, Ga K_{α} = 9.241 keV, In L_{α} = 24.210 keV, and Se K_{α} = 11.207 keV. Time-Resolved Photoluminescence (TRPL) was measured at room temperature with a Picoquant photodetector with a TimeHarp 260 single photon counter. The excitation intensity was ~ 0.1 W.cm⁻² and the frequency was 3 MHz with an excitation wavelength of 532 nm. The one dimensional SCAPS was used following Violas et al. baseline⁷¹ to fit the experimental J - V curves allowing for an in-depth discussion of the obtained electrical performance of the produced devices.

DATA AVAILABILITY

The manuscript data that support the findings of this study are available from the corresponding authors upon reasonable request.

CODE AVAILABILITY

The manuscript used code that support the electrical 1D SCAPS simulations are available from the corresponding authors upon reasonable request.

Received: 12 August 2022; Accepted: 7 January 2023;

Published online: 02 February 2023

REFERENCES

- Ise, Fraunhofer Institute for Solar Energy Systems. *Photovoltaics Report*. www.ise.fraunhofer.de (2020).
- Ramanujam, J. et al. Flexible CIGS, CdTe and a-Si:H based thin film solar cells: a review. *Prog. Mat. Sci.* **110**, 100619 (2020).
- Feurer, T. et al. Progress in thin film CIGS photovoltaics—research and development, manufacturing, and applications. *Prog. Photovol.* **25**, 645–667 (2017).
- Kessler, F. & Rudmann, D. Technological aspects of flexible CIGS solar cells and modules. *Sol. Energy* **77**, 685–695 (2004).
- Reinhard, P. et al. Review of progress toward 20% efficiency flexible CIGS solar cells and manufacturing issues of solar modules. *IEEE J. Photovol.* **3**, 572–580 (2013).
- Hagmann, M. *Flexible Solar Cells with Record Efficiency of 22.2%*. <https://www.empa.ch/web/s604/solarzellen-rekord> (2022).
- Nakamura, M. et al. Cd-free Cu(In,Ga)(Se,S)₂ thin-film solar cell with record efficiency of 23.35%. *IEEE J. Photovol.* **9**, 1863–1867 (2019).
- Fthenakis, V. Sustainability of photovoltaics: the case for thin-film solar cells. *Renew. Sustain. Energy Rev.* **13**, 2746–2750 (2009).
- Gloeckler, M. & Sites, J. R. Potential of submicrometer thickness Cu(In,Ga)Se₂ solar cells. *J. Appl. Phys.* **98**, 103703 (2005).
- Amin, N., Chelvanathan, P., Hossain, M. I. & Sopian, K. Numerical modelling of ultra thin Cu(In,Ga)Se₂ solar cells. *Energy Procedia* **15**, 291–298 (2012).
- Han, A. et al. Structure, morphology and properties of thinned Cu(In,Ga)Se₂ films and solar cells. *Semicond. Sci. Technol.* **27**, 035022 (2012).
- Cunha, J. M. V. et al. Decoupling of optical and electrical properties of rear contact CIGS solar cells. *IEEE J. Photovol.* **9**, 1857–1862 (2019).
- Bose, S. et al. Optical lithography patterning of SiO₂ layers for interface passivation of thin film solar cells. *Sol. RRL* **2**, 1800212 (2018).
- Salomé, P. M. P. et al. Passivation of interfaces in thin film solar cells: understanding the effects of a nanostructured rear point contact layer. *Adv. Mater. Interfaces* **5**, 1701101 (2018).
- Cunha, J. M. V. et al. High-performance and industrially viable nanostructured SiO_x layers for interface passivation in thin film solar cells. *Sol. RRL* **5**, 2000534 (2021).
- Lontchi, J. et al. Optimization of back contact grid size in Al₂O₃-rear-passivated ultrathin CIGS PV cells by 2-D simulations. *IEEE J. Photovol.* **10**, 1908–1917 (2020).
- Bose, S. et al. A morphological and electronic study of ultrathin rear passivated Cu(In,Ga)Se₂ solar cells. *Thin Solid Films* **671**, 77–84 (2019).
- Schiff, H. Nanoimprint lithography: an old story in modern times? A review. *J. Vac. Sci. Technol. B* **26**, 458 (2008).
- Chou, S. Y., Krauss, P. R. & Renstrom, P. J. Imprint of sub-25 nm vias and trenches in polymers. *Appl. Phys. Lett.* **67**, 3114–3116 (1995).
- Zhou, W. et al. Enhanced efficiency of light emitting diodes with a nano-patterned gallium nitride surface realized by soft UV nanoimprint lithography. *Nanotechnol.* **21**, 205304 (2010).
- Liu, Y. et al. The construction of Si₂Sb₂Te₅ electrical probe storage based on UV nanoimprint lithography. *Nanotechnol.* **20**, 315304 (2009).
- Ahn, S. H. & Guo, L. J. Large-area roll-to-roll and roll-to-plate nanoimprint lithography: a step toward high-throughput application of continuous nanoimprinting. *ACS Nano* **3**, 2304–2310 (2009).
- Park, S. K. et al. Electrical characteristics of poly(3-hexylthiophene) thin film transistors printed and spin-coated on plastic substrates. *Synth. c. Met.* **139**, 377–384 (2003).
- Chang, J.-F. et al. Enhanced mobility of Poly(3-hexylthiophene) transistors by spin-coating from high-boiling-point solvents. *Chem. Mater.* **16**, 4772–4776 (2004).
- Bhingardive, V., Menahem, L. & Schwartzman, M. Soft thermal nanoimprint lithography using a nanocomposite mold. *Nano Res.* **11**, 2705–2714 (2018).
- Ju, S. et al. Fabrication of perovskite solar cell with high short-circuit current density (JSC) using moth-eye structure of SiO_x. *Nano Res.* **13**, 1156–1161 (2020).
- Wang, C. et al. Discretely-supported nanoimprint lithography for patterning the high-spatial-frequency stepped surface. *Nano Res* **14**, 2606–2612 (2021).
- Essig, S., Paetel, S., Friedmeier, T. M. & Powalla, M. Challenges in the deposition of (Ag,Cu)(In,Ga)Se₂ absorber layers for thin-film solar cells. *J. Phys. Mater.* **4**, 024003 (2021).
- Edoff, M. et al. High V_{oc} in (Cu,Ag)(In,Ga)Se₂ solar cells. *IEEE J. Photovol.* **7**, 1789–1794 (2017).
- Yang, S.-C. et al. Silver-promoted high-performance (Ag,Cu)(In,Ga)Se₂ thin-film solar cells grown at very low temperature. *Sol. RRL* **5**, 2100108 (2021).
- Oliveira, K. et al. in *2021 IEEE 48th Photovoltaic Specialists Conference (PVSC)*. 1–8 (IEEE, 2022).
- Graczyk, M. et al. Nanoimprint stamps with ultra-high resolution: optimal fabrication techniques. *Microelectron. Eng.* **190**, 73–78 (2018).
- Oliveira, A. J. N. et al. Encapsulation of nanostructures in a dielectric matrix providing optical enhancement in ultrathin solar cells. *Sol. RRL* **4**, 2000310 (2020).
- de Wild, J. et al. High Voc upon KF post-deposition treatment for ultrathin single-stage coevaporated Cu(In,Ga)Se₂ solar cells. *ACS Appl. Energy Mater.* **2**, 6102–6111 (2019).
- Lopes, T. S. et al. Rear optical reflection and passivation using a nanopatterned metal/dielectric structure in thin-film solar cells. *IEEE J. Photovol.* **9**, 1421–1427 (2019).
- Salomé, P. M. P., Rodriguez-Alvarez, H. & Sadewasser, S. Incorporation of alkali metals in chalcogenide solar cells. *Sol. Energy Mater. Sol. Cells* **143**, 9–20 (2015).
- Umehara, T., Nakada, K. & Yamada, A. Impact of roll-over-shaped current–voltage characteristics and device properties of Ag(In,Ga)Se₂ solar cells. *Jpn. J. Appl. Phys.* **56**, 012302 (2016).
- Salomé, P., Fjällström, V., Hultqvist, A. & Edoff, M. Na doping of CIGS solar cells using low sodium-doped Mo layer. *IEEE J. Photovol.* **3**, 509–513 (2013).
- Mansfield, L. M. et al. Efficiency increased to 15.2% for ultra-thin Cu(In,Ga)Se₂ solar cells. *Prog. Photovol.* **26**, 949–954 (2018).
- Yang, S. et al. Bandgap optimization of submicron-thick Cu(In,Ga)Se₂ solar cells. *Prog. Photovol.* **23**, 1157–1163 (2015).
- Oliveira, A. J. N. et al. Optoelectronic simulations for novel light management concepts in Cu(In,Ga)Se₂ solar cells. *Phy. Sim. Photonic. Eng. Photovol. Devices X*. **11681**, 8–27 (SPIE, 2021).
- Oliveira, A. J. N., Teixeira, J. P., Ramos, D., Fernandes, P. A. & Salomé, P. M. P. Exploiting the optical limits of thin-film solar cells: a review on light management strategies in Cu(In,Ga)Se₂. *Adv. Photonics* **3**, 2100190 (2022).
- Lei, Y.-G., Ng, K.-M., Weng, L.-T., Chan, C.-M. & Li, L. XPS C 1s binding energies for fluorocarbon–hydrocarbon microblock copolymers. *Surf. Interface Anal.* **35**, 852–855 (2003).
- Park, S., Sun, C. & Purtell, R. J. A mechanistic study of SF₆/O₂ reactive ion etching of molybdenum. *J. Vac. Sci. Technol. B: Microelectron. Process. Phenom.* **5**, 1372–1373 (1987).
- Salomé, P. M. P. et al. Incorporation of Na in Cu(In,Ga)Se₂ thin-film solar cells: a statistical comparison between Na from soda-lime glass and from a precursor layer of NaF. *IEEE J. Photovol.* **4**, 1659–1664 (2014).
- Salomé, P. M. P. et al. The effect of Mo back contact ageing on Cu(In,Ga)Se₂ thin-film solar cells. *Prog. Photovol.* **22**, 83–89 (2014).
- Vermang, B. et al. Introduction of Si PERC rear contacting design to boost efficiency of Cu(In,Ga)Se₂ solar cells. *IEEE J. Photovol.* **4**, 1644–1649 (2014).
- Vermang, B., Fjällström, V., Pettersson, J., Salomé, P. & Edoff, M. Development of rear surface passivated Cu(In,Ga)Se₂ thin film solar cells with nano-sized local rear point contacts. *Sol. r. Energy Mater. Sol. Cells* **117**, 505–511 (2013).
- Rostan, P. J., Mattheis, J., Bilger, G., Rau, U. & Werner, J. H. Formation of transparent and ohmic ZnO:Al/MoSe₂ contacts for bifacial Cu(In,Ga)Se₂ solar cells and tandem structures. *Thin Solid Films* **480–481**, 67–70 (2005).
- Pianezzi, F. et al. Electronic properties of Cu(In,Ga)Se₂ solar cells on stainless steel foils without diffusion barrier. *Prog. Photovol.* **20**, 253–259 (2012).
- Wuerz, R., Eicke, A., Kessler, F. & Pianezzi, F. Influence of iron on the performance of CIGS thin-film solar cells. *Sol. Energy Mater. Sol. Cells* **130**, 107–117 (2014).
- Pianezzi, F. et al. Influence of Ni and Cr impurities on the electronic properties of Cu(In,Ga)Se₂ thin film solar cells. *Prog. Photovol.* **23**, 892–900 (2015).
- Oueslati, S. et al. Study of (Ag_xCu_{1-x})₂ZnSn(S,Se)₄ monograins synthesized by molten salt method for solar cell applications. *Sol. Energy* **198**, 586–595 (2020).
- Gessert, T. A. et al. In *2011 37th IEEE Photovoltaic Specialists Conference* 001271–001274 (IEEE, 2011).
- Curado, M. A. et al. Front passivation of Cu(In,Ga)Se₂ solar cells using Al₂O₃: Sulprits and benefits. *Appl. Mat. Today* **21**, 100867 (2020).
- Carron, R. et al. Advanced Alkali Treatments for High-Efficiency Cu(In,Ga)Se₂ Solar Cells on Flexible Substrates. *Adv. Energy Mat.* **9**, 1900408 (2019).
- Harris, K. D., Elias, A. L. & Chung, H.-J. Flexible electronics under strain: a review of mechanical characterization and durability enhancement strategies. *J. Mater. Sci.* **51**, 2771–2805 (2016).
- Mao, L., Meng, Q., Ahmad, A. & Wei, Z. Mechanical analyses and structural design requirements for flexible energy storage devices. *Adv., Energy Mat.* **7**, 1700535 (2017).
- Gerthoffer, A. et al. CIGS solar cells on flexible ultra-thin glass substrates: characterization and bending test. *Thin Solid Films* **592**, 99–104 (2015).
- Rathore, S. & Singh, A. Bending fatigue damage reduction in indium tin oxide (ITO) by polyimide and ethylene vinyl acetate encapsulation for flexible solar cells. *Eng. Res. Express* **2**, 015022 (2020).

61. Pandey, M. et al. Dependence of ITO-coated flexible substrates in the performance and bending durability of perovskite solar cells. *Adv. Eng. Mat.* **21**, 1900288 (2019).
62. Peng, C.-Y. et al. Strained growth of aluminum-doped zinc oxide on flexible glass substrate and degradation studies under cyclic bending conditions. *IEEE Trans. Device Mater. Reliab.* **14**, 121–126 (2014).
63. Peng, C.-Y., Hamasha, M. M., VanHart, D., Lu, S. & Westgate, C. R. Electrical and optical degradation studies on AZO thin films under cyclic bending conditions. *IEEE Trans. Device Mater. Reliab.* **13**, 236–244 (2013).
64. Tsai, W.-C. et al. Flexible high performance hybrid AZO/Ag-nanowire/AZO sandwich structured transparent conductors for flexible Cu(In,Ga)Se₂ solar cell applications. *J. f. Mat. Chem. A* **4**, 6980–6988 (2016).
65. Liu, Y. et al. Draw-spun, photonically annealed Ag fibers as alternative electrodes for flexible CIGS solar cells. *Sci. Technol. Adv. Mater.* **20**, 26–34 (2019).
66. Cunha, J. M. V. et al. Insulator materials for interface passivation of Cu(In,Ga)Se₂ thin films. *IEEE J. Photovolt.* **8**, 1313–1319 (2018).
67. Yanaka, M., Tsukahara, Y., Nakaso, N. & Yanaka, M. Cracking phenomena of brittle films in nanostructure composites analysed by a modified shear lag model with residual strain. *J. Mat. Sci.* **33**, 2111–2119 (1998).
68. Eriksson, T., Yamada, S., Venkatesh Krishnan, P., Ramasamy, S. & Heidari, B. High volume nanoimprint lithography on III/V substrates: Imprint fidelity and stamp lifetime. *Microelectron. Eng.* **88**, 293–299 (2011).
69. Llobet, J. et al. Automated characterisation and analysis of large arrays of nanostructures fabricated at wafer scale. *Precis. Eng.* **60**, 320–325 (2019).
70. Lindahl, J. et al. Inline Cu(In,Ga)Se₂ co-evaporation for high-efficiency solar cells and modules. *IEEE J. Photovolt.* **3**, 1100–1105 (2013).
71. Violas, A. F. et al. Will ultrathin CIGS solar cells overtake the champion thin-film cells? Updated SCAPS baseline models reveal main differences between ultrathin and standard CIGS. *SolEnergy Mater. Sol. Cells* **243**, 111792 (2022).

ACKNOWLEDGEMENTS

This work was funded in part by the Fundação para a Ciência e a Tecnologia (FCT) under Grants 2020.04564.BD, IF/00133/2015, PD/BD/142780/2018, SFRH/BD/146776/2019, UIDB/04564/2020 and UIDP/04564/2020, 2020.07073.BD, as well as through the projects NovaCell (PTDC/CTM-CTM/28075/2017), CASOLEM (028917) “Correlated Analysis of Inorganic Solar Cells in and outside an Electron Microscope”, and InovSolarCells (PTDC/FISMAC/29696/2017) co-funded by FCT and the ERDF through COMPETE2020. And by the European Union’s Horizon 2020 research and innovation programme under the grants agreements N°. 720887 (ARCI-GS-M project) and grand agreement N°.715027 (Uniting PV). The Special Research Fund (BOF) of Hasselt University is also acknowledged. P.M.P.S. and P.A.F. would like to acknowledge FCT for the support of the project FCT UIDB/04730/2020. This work was developed within the scope of the project i3N, UIDB/50025/2020 & UIDP/50025/2020, financed by national funds through the FCT/MEC. The authors also acknowledge the support of Carlos Calaza in the fabrication for the 200 mm Si point contact stamp.

AUTHOR CONTRIBUTIONS

T.S.L., J.P.T. and P.M.P.S. conceived, designed and supervised the research. Electron beam lithography was performed by J.B. P.C.S. provided assistance for the 200 mm stamp fabrication. J.R. and Y.Z. provided assistance in the NIL process. SEM measurements were performed by K.O. AFM analysis was performed by B.R.F. Electrical measurements were performed and analysed by M.A.C., J.M.V.C., and J.R.S.B. Data interpretation of TRPL was done by M.A.C. and J.P.T. SCAPS simulations were performed by A.V. and A.J.N.O. TEM measurements, analysis and sample preparation were performed by M.M., I.Ç. and F.L.D. Bending measurements were performed and analysed by B.R.F. CIGS absorber layer growth and subsequent layers were performed by W.C.C. and M.E. Flexible substrates and assistance in flexible processing were provided by K.T. and E.N. G.B., P.A.F., B.V. and P.M.P.S. secured funding. All authors contributed to the final version of manuscript. The manuscript was written by T.S.L., J.P.T. and P.M.P.S. and they also coordinated co-authors inputs, reviews and suggestions.

COMPETING INTERESTS

The authors declare no competing interests.

ADDITIONAL INFORMATION

Correspondence and requests for materials should be addressed to T. S. Lopes or J. P. Teixeira.

Reprints and permission information is available at <http://www.nature.com/reprints>

Publisher’s note Springer Nature remains neutral with regard to jurisdictional claims in published maps and institutional affiliations.



Open Access This article is licensed under a Creative Commons Attribution 4.0 International License, which permits use, sharing, adaptation, distribution and reproduction in any medium or format, as long as you give appropriate credit to the original author(s) and the source, provide a link to the Creative Commons license, and indicate if changes were made. The images or other third party material in this article are included in the article’s Creative Commons license, unless indicated otherwise in a credit line to the material. If material is not included in the article’s Creative Commons license and your intended use is not permitted by statutory regulation or exceeds the permitted use, you will need to obtain permission directly from the copyright holder. To view a copy of this license, visit <http://creativecommons.org/licenses/by/4.0/>.

© The Author(s) 2023